

Defect engineering by synchrotron radiation X-rays in CeO₂ nanocrystals

Tai-Sing Wu,^a Leng-You Syu,^a Shih-Chang Weng,^b Horng-Tay Jeng,^{a,c}
Shih-Lin Chang^{a,b} and Yun-Liang Soo^{a,b,*}

^aDepartment of Physics, National Tsing Hua University, Hsinchu, Taiwan, ^bNational Synchrotron Radiation Research Center, Hsinchu, Taiwan, and ^cInstitute of Physics, Academia Sinica, Taipei, Taiwan.

*Correspondence e-mail: soo@phys.nthu.edu.tw

Received 18 January 2018

Accepted 3 June 2018

Edited by A. F. Craievich, University of São Paulo, Brazil

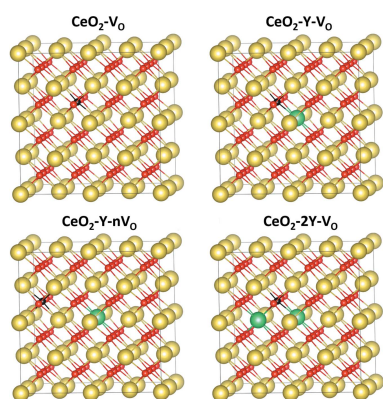
Keywords: X-ray irradiation; defect engineering; XANES; DFT.

Supporting information: this article has supporting information at journals.iucr.org/s

This work reports an unconventional defect engineering approach using synchrotron-radiation-based X-rays on ceria nanocrystal catalysts of particle sizes 4.4–10.6 nm. The generation of a large number of oxygen-vacancy defects (OVDs), and therefore an effective reduction of cations, has been found in CeO₂ catalytic materials bombarded by high-intensity synchrotron X-ray beams of beam size 1.5 mm × 0.5 mm, photon energies of 5.5–7.8 keV and photon fluxes up to 1.53×10^{12} photons s⁻¹. The experimentally observed cation reduction was theoretically explained by a first-principles formation-energy calculation for oxygen vacancy defects. The results clearly indicate that OVD formation is mainly a result of X-ray-excited core holes that give rise to valence holes through electron down conversion in the material. Thermal annealing and subvalent Y-doping were also employed to modulate the efficiency of oxygen escape, providing extra control on the X-ray-induced OVD generating process. Both the core-hole-dominated bond breaking and oxygen escape mechanisms play pivotal roles for efficient OVD formation. This X-ray irradiation approach, as an alternative defect engineering method, can be applied to a wide variety of nanostructured materials for physical-property modification.

1. Introduction

Structural changes in condensed matter caused by X-ray irradiation are often categorized as radiation damage, a nuisance in materials characterization using synchrotron radiation. Irradiation of X-rays can break chemical bonds, causing constituent atoms to escape and therefore generating vacancy defects in the materials. The structural defects can severely hinder the expected performance of the materials in applications. However, the advent of defect engineering in catalytic materials has offered an unprecedented opportunity to turn such adverse effects into a useful technique. Defect engineering has recently been demonstrated as a rather effective approach for enhancing the catalytic activity of ceria nanostructures used in catalytic oxidation (Lawrence *et al.*, 2011). By thermally annealing ceria catalysts in a low-pressure or reductive atmosphere, a large number of oxygen vacancy defects (OVDs) can be introduced into the materials, giving rise to effective reduction of the constituent Ce ions. The increased concentration of subvalent Ce³⁺ ions in the reduced catalyst facilitates efficient oxygen uptake and release in a Mars-van Krevelen mechanism, resulting in enhanced catalytic activity. However, thermal annealing may incur agglomeration of nanoparticles, severely reducing the surface-to-volume ratio of the nanoparticles and thus the reactive surface area. On the other hand, it is conceivable that the high-intensity X-ray-photon beam from a synchrotron radiation



source can be used to bombard the catalyst sample and generate OVDs without thermal annealing. As an example of the effects of X-rays on vacancies, we note that the pump and probe of phase separation and oxygen interstitial mobility in cuprate and nickelate has been reported recently (Poccia *et al.*, 2011; Bianconi *et al.*, 2018). In the present work, we investigate the creation and migration of synchrotron-X-ray induced OVDs in ceria nanocrystals.

It is worth noting that a reduction effect on the CeO₂ surface has been observed previously in an in-house X-ray photoelectron spectroscopy (XPS) device using an Al K α X-ray source under ultra-high vacuum (Paparazzo, 1990, 1991). Several possible factors such as high temperature, high vacuum, core-hole effect, damage caused by secondary photoelectrons and the formation of hydroxyl species were proposed to account for the generation of OVDs on the X-ray-irradiated surface (Paparazzo, 1990, 1991; El Fallah *et al.*, 1995; Rao & Shripathi, 1997; Paparazzo & Ingo, 1998). To elucidate the origin of oxygen-vacancy formation caused by X-ray irradiation, we have performed X-ray absorption near-edge structure (XANES) measurements on samples treated with X-ray irradiation of different exposure times, photon energies and flux, as well as samples doped with trivalent Y. A first-principles calculation using density functional theory (DFT) was employed to estimate the formation energies of ceria with OVDs for samples with different Y concentrations under X-ray irradiation.

2. Experimental

A polyol method was employed to prepare CeO₂ nanocrystal samples (Wu *et al.*, 2015). The as-made samples were then annealed in O₂ at 300°C and 500°C for 30 min, respectively. Two Y-doped samples, Y1 and Y2, with Y concentrations of 22.6% and 34.4% determined from inductively coupled plasma mass spectrometry (ICPMS), were also synthesized and annealed in O₂ at 300°C for 30 min. As shown in Fig. S1 (see supporting information), the X-ray powder diffraction (XRD) patterns for all samples match well with that of cubic CeO₂ at the (111), (200), (220), (311), (222), (400), (331) and (420) Bragg peaks. No yttrium oxide phase was detected. The crystallite sizes, calculated using the Scherrer equation, are 4.4 nm, 4.5 nm and 10.6 nm for the as-made, 300°C- and 500°C-annealed CeO₂ samples, respectively. For the 300°C-annealed Y-doped samples Y1 and Y2, the crystallite size was determined to be ~4.2 nm.

To study the effects of X-ray irradiation, a thin layer of nanoparticles was dispersed onto a Kapton tape and then an area of 1.5 mm \times 0.5 mm of the layer was exposed to monochromated synchrotron X-rays of a chosen photon energy for a selected period of time for each sample in air. The thickness of the powder layer was carefully adjusted such that all of the samples exhibit the same edge-jump height ($\mu\Delta x \simeq 0.35$) at the Ce L₃-edge. To obtain the dependence of material variations on the irradiation time, the as-made (unannealed) CeO₂ sample was irradiated at a photon energy of 7 keV with a fixed photon flux of 1.4×10^{12} photons s⁻¹. For measuring the

dependence on photon energy, a fixed photon flux of around 3.4×10^{11} photons s⁻¹ was used with a fixed exposure time of 2 h. To determine the dependence on photon flux, X-ray attenuators were used to vary the photon flux, with the photon energy and exposure time fixed at 7 keV and 1 h, respectively. After X-ray irradiation, Ce L₃-edge XANES was measured in order to monitor the evolution of the peaks ascribed to Ce³⁺ and Ce⁴⁺, as well as the Ce³⁺ concentration calculated therefrom. To ensure that the XANES data were measured exclusively from the irradiated sample area, both the horizontal and vertical dimensions of the X-ray beam were reduced to half of those used for irradiation treatment by using a set of X-ray slits. Also, an X-ray attenuator was used to reduce the X-ray intensity during XANES measurements such that the difference between two consecutive XANES scans was negligible, making sure that the intensity of the incident X-ray beam used for XANES measurements is not enough to incur material changes that are as substantial as those incurred by the X-ray irradiation treatment. All Ce XANES were performed in transmission mode using a set of gas ionization chambers at beamline BL07A of the Taiwan Light Source at the National Synchrotron Radiation Research Center (NSRRC).

3. Results and discussion

Fig. 1(a) shows the Ce L₃-edge XANES spectra of the as-made (unannealed) CeO₂ sample irradiated for different exposure times. It is clear that the peak ascribed to Ce³⁺ increases with the exposure time. The percentage of Ce³⁺ was quantitatively extracted from the XANES data by curve-fitting the spectrum with an arctangent function for the edge jump and Gaussian functions for the peaks. The fraction of Ce³⁺ was determined using the following equation:

$$[\text{Ce}^{3+}] = \text{Ce}^{3+} / (\text{Ce}^{3+} + \text{Ce}^{4+}),$$

where Ce³⁺ and Ce⁴⁺ are the sums of the integrated peak areas related to the Ce³⁺ and Ce⁴⁺ XANES signals, respectively. Details on the curve-fitting method used for extracting Ce³⁺

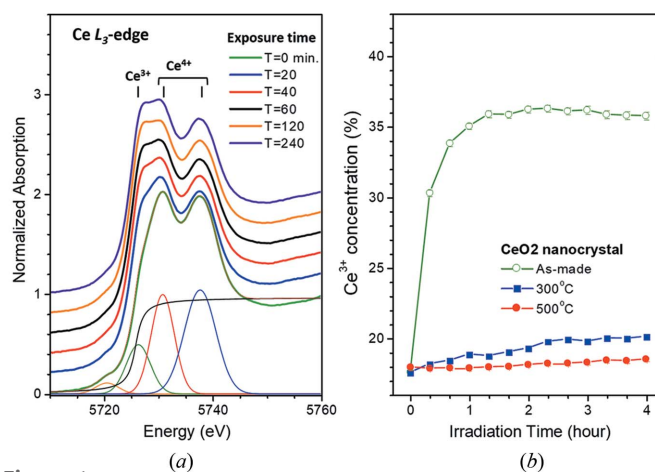


Figure 1 (a) Ce L₃-edge XANES data of the as-made CeO₂ sample irradiated by X-rays for different time durations. (b) Plot of the Ce³⁺ concentration versus irradiation time.

concentration from XANES spectra have been reported elsewhere (Wu *et al.*, 2016). As shown in Fig. 1(b), the Ce^{3+} concentration obtained from curve-fitting the XANES spectrum of the as-made sample increases rapidly from 17.6% and saturates at 36.2% as the exposure time increases. For the 300°C-annealed sample, the increase in the Ce^{3+} concentration with the exposure time proceeds at a much slower rate and saturates at a much lower value. Furthermore, the Ce^{3+} concentration for the 500°C-annealed sample is almost unchanged after 4 h of X-ray irradiation.

It is conceivable that the irradiation of CeO_2 by X-rays can break some Ce–O bonds, releasing O atoms from the sample, and thus transforming some of the Ce^{4+} ions into Ce^{3+} ions in the ceria sample. The increased rate of saturation and the high saturation value of the Ce^{3+} concentration is therefore highly dependent on the efficiency of the bond breaking and the oxygen escape mechanism. As revealed in the XRD data, the thermal annealing process can increase the crystallite size of the sample. After 500°C annealing, the crystallite size of the sample increases from the as-made value of 4.4 nm to 10.6 nm. Therefore, the O atoms inside the crystallites need to travel a longer distance when escaping from the crystallites. In addition, the improved crystallinity attributed to thermal annealing also makes it more difficult for O atoms to migrate through the host matrix. Both the increase in crystallite size and improvement in crystallinity can hamper the reduction of Ce and therefore substantially restrain the increase in the Ce^{3+} concentration in the annealed samples.

As a side remark, we note that the potential interaction between ambient oxygen with ceria at elevated temperatures may also affect the Ce^{3+} concentration in the nanoparticles as indicated by XPS studies (El Fallah *et al.*, 1995; Holgado *et al.*, 2000; Qiu *et al.*, 2006). However, our X-ray irradiation treatment was carried out at room temperature in an air-conditioned hutch with adequate ventilation. The effects pertaining to the dissociation of O_2 molecules into atomic oxygen on the particle surface that diffuse to quench OVDs are rather limited and may be neglected (Li *et al.*, 1990). Therefore, our investigation was only focused on the breakaway and migration of O atoms from the oxygen sites in the nanoparticles caused by X-ray irradiation. Also, to monitor crystal structural changes caused by X-ray irradiation, the Ce XANES spectra and XRD patterns of the as-made CeO_2 sample irradiated for different time durations were measured. As shown in Fig. S2, despite the increase of oxygen-vacancy concentration from X-ray irradiation, the sample remains a CeO_2 $Fm\bar{3}m$ cubic structure. A slightly increased lattice parameter was observed as a result of oxygen-vacancy-induced structural relaxation.

The importance of efficient oxygen migration for X-ray-induced Ce^{3+} -concentration increase can be further demonstrated by the effects of Y doping. When a trivalent Y dopant atom replaces a tetravalent Ce atom in the CeO_2 host, an OVD is effectively introduced into the matrix lattice (Liyang *et al.*, 2014). The breakaway O atoms produced by X-ray irradiation can travel through the host lattice by swapping sites with such Y-dopant-related OVDs, leaving behind reduced cerium ions, namely Ce^{3+} . It is worth noting that, as

revealed by the DFT calculations described later in this paper, the Y dopant atoms can also lower the formation energy of oxygen vacancies in doped ceria and therefore raise the saturation concentration of Ce^{3+} . The migration energy for an oxygen ion to travel through the Y–Ce edge is close to that through the Ce–Ce edge (Nakayama & Martin, 2009; Genreith-Schriever *et al.*, 2015). The similar ionic radii of Y^{3+} and Ce^{4+} also warrants that the Y doping only incurs limited structural deformation. Therefore, in comparison with other trivalent ions such as those of lanthanides, the Y^{3+} doping is more suitable for studying the correlation between efficient oxygen migration and OVDs. The dependence of the Ce^{3+} concentration on X-ray exposure time for the Y-doped ceria samples annealed at 300°C, Y₁ and Y₂, was measured and compared with that for the 300°C-annealed pure ceria sample. As shown in Fig. 2(a), the Ce^{3+} concentration indeed increases at a faster rate and saturates at a higher concentration for the sample with higher Y concentration under X-ray irradiation.

To further investigate the bond-breaking mechanism, the dependence of the Ce^{3+} concentration on X-ray photon energy and photon flux were individually studied for the as-made sample. For the dependence on photon energy, as shown in Fig. 2(b), the curve representing the Ce^{3+} concentration *versus* photon energy exhibits a step-like rise near the Ce L_3 absorption edge. Since a core hole is generated in a Ce atom when it absorbs a photon of energy above the Ce L_3 -edge, it appears that the X-ray-induced reduction, represented by the Ce^{3+} concentration increase, is closely related to the effect of core holes. For the dependency of the Ce^{3+} concentration on photon flux, as shown in Fig. 2(c), the Ce^{3+} concentration first increases linearly with photon flux then abruptly rises and finally reaches the saturation concentration. We speculate that the nonlinear regime of the curve may arise from the possible

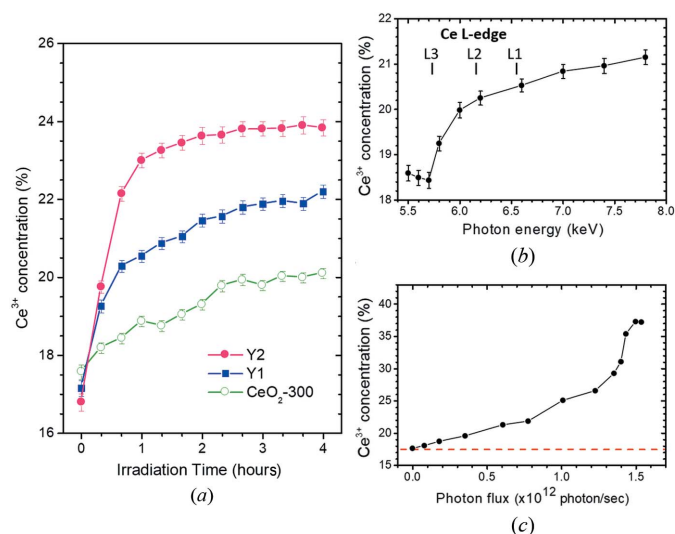


Figure 2
(a) Ce^{3+} concentration obtained from Ce L_3 -edge XANES data of samples Y1, Y2 and a 300°C-annealed CeO_2 sample with different X-ray irradiation times. (b) Plot of the Ce^{3+} concentration *versus* photon energy for the as-made CeO_2 sample. (c) Plot of the Ce^{3+} concentration *versus* photon flux for the as-made CeO_2 sample.

creation of two core holes in a small area of the sample that lead to the accelerated formation of oxygen vacancies.

It is generally recognized that the Ce^{4+} ions of CeO_2 are in a mixed electronic configuration of $4f^0$ and $4f^1L$, where L represents the electron hole in the O $2p$ state (Bianconi *et al.*, 1987; Kaindl *et al.*, 1988; Soldatov *et al.*, 1994). A recent high-pressure study on CeO_2 suggests that there are 0.35 electrons remaining in the localized Ce $4f$ state (Lipp *et al.*, 2016). In principle, the creation of the Ce core holes by X-ray irradiation can enhance the attraction between Ce and valence electrons, making the valence electrons more likely to occupy the localized Ce $4f$ state, and therefore break the Ce–O bond. However, the core-hole lifetime in the femtosecond time scale is too short for the inter-atomic events in the picosecond time scale (Drescher *et al.*, 2002; Sciaini *et al.*, 2009; Gulde *et al.*, 2014), such as the oxygen migration required for the CeO_2 reduction process, to occur. On the other hand, valence holes generated from core-holes through a series of Auger decays have much longer lifetimes in the nanosecond time scale (Ozawa *et al.*, 2014), as well as longer Coulombic attraction, and therefore can replace the core-holes for the bond-breaking role in CeO_2 reduction.

The effects of valence holes on the formation of oxygen vacancies in pure and Y-doped CeO_2 were theoretically studied with DFT calculations using the VASP code (Kresse & Furthmüller, 1996). The projector augmented-wave (PAW) method and the generalized gradient approximation (GGA) within the parameterization of Perdew–Burke–Ernzerhof (PBE) (Perdew *et al.*, 1996) were employed in the calculation. The valence electrons (Ce: $5s^25p^66s^24f^15d^1$, (Y: $4s^24p^65s^24d^1$) and (O: $2s^22p^4$) were expanded in a plane-wave basis with a kinetic-energy cutoff of 400 eV. A GGA+ U method with $U = 5$ eV applied to the Ce $4f$ -states was used for the corrections of on-site Coulombic interactions (Andersson *et al.*, 2007; Zacherle *et al.*, 2013).

The initial structural model used for the DFT calculation was constructed from a $2 \times 2 \times 2$ supercell of CeO_2 . As shown in Fig. 3(a), an O atom was removed from the supercell to mimic the formation of an oxygen vacancy. For the lightly Y-doped CeO_2 , a Ce atom was replaced by a Y atom with an oxygen vacancy on either the nearest neighbouring oxygen site (Fig. 3b) or the next nearest neighbouring oxygen site (Fig. 3c). For the heavily Y-doped ceria, two Ce atoms were replaced by Y atoms with one oxygen vacancy in between, as shown in Fig. 3(d). The existence of valence holes in the sample was imposed on the structural model by removing various numbers of valence electrons from the supercell in the calculation.

A $4 \times 4 \times 4$ Monkhorst-Pack k -point grid was used for geometry optimization for all structural models. The atomic coordinates and the lattice parameters were optimized until the maximum force on each atom was less than $0.02 \text{ eV } \text{Å}^{-1}$. The formation energies of oxygen vacancies $E_{\text{V}_\text{O}}^{\text{F}}$ were calculated using the following equation:

$$E_{\text{V}_\text{O}}^{\text{F}}(q) = E_{\text{T}}(\text{Y}_n\text{Ce}_{32-n}\text{O}_{63}, q) - E_{\text{T}}(\text{Y}_n\text{Ce}_{32-n}\text{O}_{64}, q) + \frac{1}{2} E_{\text{T}}(\text{O}_2)$$

Table 1

Oxygen vacancy formation energy (eV) in different models with various numbers of electrons removed. See Fig. 3 for a schematic view of the structural models.

Number of electrons removed	$\text{CeO}_2\text{-V}_\text{O}$	$\text{CeO}_2\text{-Y-nV}_\text{O}$	$\text{CeO}_2\text{-Y-V}_\text{O}$	$\text{CeO}_2\text{-2Y-V}_\text{O}$
0	2.74	1.02	0.82	−1.09
1	1.13	−0.60	−0.86	−1.14
2	−0.61	−0.65	−0.91	−1.16

where $E_{\text{T}}(\text{Y}_n\text{Ce}_{32-n}\text{O}_{63}, q)$ and $E_{\text{T}}(\text{Y}_n\text{Ce}_{32-n}\text{O}_{64}, q)$ are the total energies of the optimized supercells with and without oxygen vacancies, respectively, q is the number of electrons removed from the supercell, and $E_{\text{T}}(\text{O}_2)$ is the total energy for the triplet ground state of an optimized O_2 molecule in the gas phase.

The oxygen-vacancy formation energies in all of the discussed defect structures are summarized in Table 1. We note that the oxygen-vacancy formation energy of CeO_2 obtained from our calculation (2.74 eV) is close to the value reported previously (Andersson *et al.*, 2007; Zacherle *et al.*, 2013). The oxygen vacancy formation energy decreases to 1.13 eV when a valence electron is removed by X-ray irradiation. When an O atom is removed from CeO_2 , the two electrons left on the oxygen vacancy site will be transferred to the two nearest Ce atoms, forming Ce $4f^1$ defect states

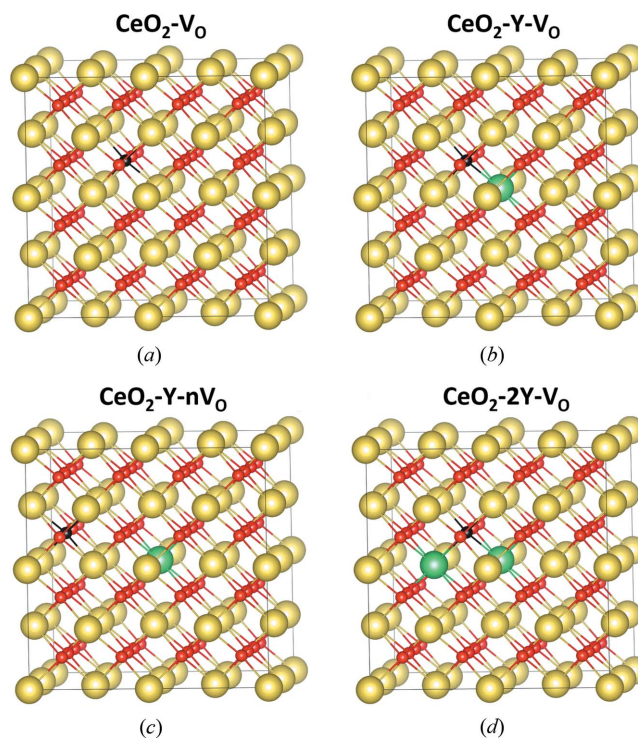


Figure 3

Schematic view of V_O (a) in pure CeO_2 , (b) on the nearest neighbouring oxygen site surrounding Y in Y-doped CeO_2 , (c) on the next nearest neighbouring oxygen site surrounding Y in Y-doped CeO_2 and (d) on an oxygen site in between two Y dopant atoms. The large yellow spheres, large green spheres, small red spheres and small black spheres represent the Ce, Y and O atoms and V_O , respectively.

(Jerratsch *et al.*, 2011). However, as a valence hole is created by X-ray irradiation, only one electron will be transferred, giving rise to a largely lowered Coulomb energy. When two valence holes are generated by X-ray irradiation, the formation energy is further reduced to a negative value of -0.61 eV and oxygen-vacancy formation starts to be energetically favoured in CeO₂.

When a tetravalent Ce cation is replaced by a trivalent Y atom in Y-doped CeO₂, the valence electron of the system is effectively one less than that of pure ceria and only one electron is to be transferred to Ce upon oxygen-vacancy formation. Therefore, the formation energies of 0.82 eV and 1.02 eV for oxygen-vacancy formation on the nearest and next nearest neighbouring oxygen sites surrounding Y, respectively, are much lower than the pure ceria value of 2.74 eV. In the model with two Y dopant atoms, the formation energy of an oxygen vacancy located between two Y atoms has a negative value of -1.09 eV, representing spontaneous formation of oxygen vacancies even without X-ray irradiation.

4. Conclusions

We have experimentally and theoretically demonstrated that synchrotron X-ray irradiation is an annealing-free approach to engineering a large amount of OVDs into ceria nanocrystals and effectively increases the Ce³⁺ concentration in the material. Thermal annealing at elevated temperatures was found to diminish the irradiation-induced reduction because of restrained oxygen escape, arising from crystallite size increase and crystallinity improvement in ceria. On the other hand, doping of trivalent Y atoms in the ceria samples enhances the irradiation-induced reduction as there are effectively more empty sites in the ceria lattice for O atoms to escape. Since X-ray absorption generates core holes, the positive correlation between X-ray photon absorption and Ce³⁺ concentration, observed in the photon energy and photon flux scans, serves as clear experimental evidence that the X-ray-incurred OVD formation is mainly the result of X-ray-created core holes. Theoretical formation energy calculations also confirmed that Ce–O bonds can be broken to form OVDs due to the existence of valence holes generated from X-ray-created core holes through electron down conversion in the ceria samples. It appears that the bond-breaking and oxygen-escape mechanisms both play pivotal roles for efficient OVD formation. Combined with the effects of thermal annealing and subvalent ion doping, synchrotron X-ray irradiation as an effective defect engineering approach for CeO₂-containing catalysts can also be applied to a wide variety of other materials.

Funding information

The following funding is acknowledged: Ministry of Science and Technology, Taiwan (grant No. 104-2112-M-007-008-MY3 to Yun-Liang Soo).

References

- Andersson, D. A., Simak, S. I., Johansson, B., Abrikosov, I. A. & Skorodumova, N. V. (2007). *Phys. Rev. B*, **75**, 035109.
- Bianconi, A., Marcelli, A., Bendele, M., Innocenti, D., Barinov, A., Poirot, N. & Campi, G. (2018). *Condens. Matter*, **3**, 6.
- Bianconi, A., Marcelli, A., Dexpert, H., Karnatak, R., Kotani, A., Jo, T. & Petiau, J. (1987). *Phys. Rev. B*, **35**, 806–812.
- Drescher, M., Hentschel, M., Kienberger, R., Uiberacker, M., Yakovlev, V., Scrinzi, A., Westerwalbesloh, Th., Kleineberg, U., Heinzmann, U. & Krausz, F. (2002). *Nature (London)*, **419**, 803–807.
- El Fallah, J., Hilaire, L., Roméo, M. & Le Normand, F. (1995). *J. Electron Spectrosc. Relat. Phenom.* **73**, 89–103.
- Genreith-Schriever, A. R., Hebbeker, P., Hinterberg, J., Zacherle, T. & De Souza, R. A. (2015). *J. Phys. Chem. C*, **119**, 28269–28275.
- Gulde, M., Schweda, S., Storeck, G., Maiti, M., Yu, H. K., Wodtke, A. M., Schäfer, S. & Ropers, C. (2014). *Science*, **345**, 200–204.
- Holgado, J. P., Alvarez, R. & Munuera, G. (2000). *Appl. Surf. Sci.* **161**, 301–315.
- Jerratsch, J. F., Shao, X., Nilus, N., Freund, H. J., Popa, C., Ganduglia-Pirovano, M. V., Burow, A. M. & Sauer, J. (2011). *Phys. Rev. Lett.* **106**, 246801.
- Kaindl, G., Schmiester, G., Sampathkumaran, E. V. & Wachter, P. (1988). *Phys. Rev. B*, **38**, 10174–10177.
- Kresse, G. & Furthmüller, J. (1996). *Phys. Rev. B*, **54**, 11169–11186.
- Lawrence, N. J., Brewer, J. R., Wang, L., Wu, T.-S., Wells-Kingsbury, J., Ihrig, M. M., Wang, G., Soo, Y.-L., Mei, W.-N. & Cheung, C. L. (2011). *Nano Lett.* **11**, 2666–2671.
- Li, C., Domen, K., Maruya, K. & Onishi, T. (1990). *J. Catal.* **123**, 436–442.
- Lipp, M. J., Jeffries, J. R., Cynn, H., Park Klepeis, J.-H., Evans, W. J., Mortensen, D. R., Seidler, G. T., Xiao, Y. & Chow, P. (2016). *Phys. Rev. B*, **93**, 064106.
- Liyana, A. D., Perera, S. D., Tan, K., Chabal, Y. & Balkus, K. J. Jr (2014). *ACS Catal.* **4**, 577–584.
- Nakayama, M. & Martin, M. (2009). *Phys. Chem. Chem. Phys.* **11**, 3241–3249.
- Ozawa, K., Emori, M., Yamamoto, S., Yukawa, R., Yamamoto, S., Hobara, R., Fujikawa, K., Sakama, H. & Matsuda, I. (2014). *J. Phys. Chem. Lett.* **5**, 1953–1957.
- Paparazzo, E. (1990). *Surf. Sci.* **234**, L253–L258.
- Paparazzo, E. & Ingo, G. M. (1998). *J. Electron Spectrosc. Relat. Phenom.* **95**, 301–304.
- Paparazzo, E., Ingo, G. M. & Zacchetti, N. (1991). *J. Vac. Sci. Technol. A*, **9**, 1416–1420.
- Perdew, J. P., Burke, K. & Ernzerhof, M. (1996). *Phys. Rev. Lett.* **77**, 3865–3868.
- Poccia, N., Fratini, M., Ricci, A., Campi, G., Barba, L., Vittorini-Orgeas, A., Bianconi, G., Aeppli, G. & Bianconi, A. (2011). *Nat. Mater.* **10**, 733–736.
- Qiu, L., Liu, F., Zhao, L., Ma, Y. & Yao, J. (2006). *Appl. Surf. Sci.* **252**, 4931–4935.
- Rama Rao, M. V. & Shripathi, T. (1997). *J. Electron Spectrosc. Relat. Phenom.* **87**, 121–126.
- Sciaini, G., Harb, M., Kruglik, S. G., Payer, T., Hebeisen, C. T., zu Heringdorf, F. J., Yamaguchi, M., Horn-von Hoegen, M., Ernstorfer, R. & Miller, R. J. (2009). *Nature (London)*, **458**, 56–59.
- Soldatov, A. V., Ivanchenko, T. S., Della Longa, S., Kotani, A., Iwamoto, Y. & Bianconi, A. (1994). *Phys. Rev. B*, **50**, 5074–5080.
- Wu, T. S., Li, H. D., Chen, Y. W., Chen, S. F., Su, Y. S., Chu, C. H., Pao, C. W., Lee, J. F., Lai, C. H., Jeng, H. T., Chang, S. L. & Soo, Y. L. (2015). *Sci. Rep.* **5**, 15415.
- Wu, T.-S., Zhou, Y., Sabirianov, R. F., Mei, W. N., Soo, Y.-L. & Cheung, C. L. (2016). *Chem. Commun.* **52**, 5003–5006.
- Zacherle, T., Schriever, A., De Souza, R. A. & Martin, M. (2013). *Phys. Rev. B*, **87**, 134104.